

# The edge engineering of topological Bi(111) bilayer

Xiao Li,<sup>1,2,\*</sup> Hai-Wen Liu,<sup>1,2,\*</sup> Hua Jiang,<sup>3</sup> Fa Wang,<sup>1,2</sup> and Ji Feng<sup>1,2,†</sup>

<sup>1</sup>International Center for Quantum Materials, School of Physics, Peking University, Beijing 100871, China

<sup>2</sup>Collaborative Center for Quantum Materials, Peking University, Beijing, China

<sup>3</sup>Department of Physics and Jiangsu Key Laboratory of Thin Films, Soochow University, Suzhou 215006, China  
(Dated: September 19, 2018)

A topological insulator is a novel quantum state, characterized by symmetry-protected non-trivial edge/surface states. Our first-principle simulations show the significant effects of the chemical decoration on edge states of topological Bi(111) bilayer nanoribbon, which remove the trivial edge state and recover the Dirac linear dispersion of topological edge state. By comparing the edge states with and without chemical decoration, the Bi(111) bilayer nanoribbon offers a simple system for assessing conductance fluctuation of edge states. The chemical decoration can also modify the penetration depth and the spin texture of edge states. A low-energy effective model is proposed to explain the distinctive spin texture of Bi(111) bilayer nanoribbon, which breaks the spin-momentum orthogonality along the armchair edge.

PACS numbers: 71.15.Mb, 73.43.Nq, 73.20.Fz, 73.20.-r

As an insulating state with symmetry-protected gapless interface electronic modes, the topological insulator (TI) has received considerable attention recently [1–3]. The edge conduction channels of two-dimensional (2d) TI exhibits quantum spin Hall effect within bulk gap [4]. A single bilayer Bi(111) film has been predicted to be a 2d TI with a large band gap of about 0.5 eV [5–7], while other 2d TIs, such as HgTe/CdTe quantum wells [8] and InAs/GaSb quantum wells [9], have gaps of only several tens of meV at best. Recently, Bi(111) bilayer has been readily grown on Bi<sub>2</sub>Te<sub>3</sub> or Bi<sub>2</sub>Se<sub>3</sub> substrates [10–15]. Therefore, it is very promising for room-temperature TI-based devices. However, the native edges of Bi bilayer suffer from the simultaneous presence of both trivial and non-trivial edge modes [6, 12], which complicate the fundamental investigation of its topological properties and eventual applications. Similar complication had perplexed the interpretation of surface states in three-dimensional (3d) TI Bi<sub>1-x</sub>Sb<sub>x</sub> [16, 17]. Although localization in Anderson’s sense will suppress trivial conducting channels, quantitatively localizing trivial channels will still be an experimental challenge. A wide distribution of conductance induced by multiple edge states is not desirable for accurate transport measurement [6, 18, 19].

The complicated edge or surface states may be a generic problem associated with dangling bond states at the termination of 2d or 3d TIs. In this Letter, we report a first-principle analysis of chemical decoration of the edge states of Bi(111) bilayer, which, as we show, is an effective route for precise engineering of conducting edge states. We demonstrate that chemical passivation quantitatively removes the trivial edge bands in Bi bilayer nanoribbons, restoring the desired Dirac dispersion of the non-trivial edges. We further compute transport and optical signatures of the chemical decoration of the Bi bilayer edges, which can be assessed experimentally. In particular, we suggest that the Bi bilayer nanoribbons,

with and without chemical passivation, offer a simple system for assessing conductance fluctuation of edge states. Moreover, edge decoration has important consequences on the spatial distribution and spin texture of the edge states. A low-energy effective model is proposed to explain the distinctive spin texture of Bi bilayer nanoribbon, where the spin is no longer perpendicular to the momentum along the armchair edge.

We use density functional theory [20] calculations implemented in the Vienna Ab initio simulation package [21, 22] to investigate geometric and electronic structure of single Bi(111) bilayer and its nanoribbons. Computational details can be found in the Supplementary Information (S.I.) [23]. Notice that spin-orbit coupling (SOC)

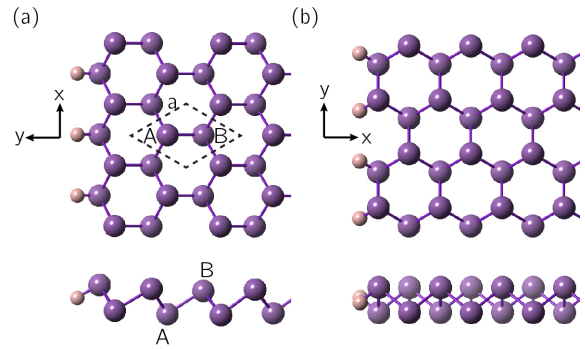


FIG. 1. The geometric structure of (a) the zigzag and (b) the armchair Bi(111) nanoribbon. Up: The top view. Down: The side view. The primitive cell of single bilayer sheet, bounded by dashed lines, are also shown. The zigzag and armchair edges are perpendicular to each other, which are along x- and y-axis of the Bi(111) sheet, respectively. The hydrogen-terminated edges shown in the figure are the most stable structure of hydrogen adsorption. The iodine-terminated nanoribbons have the similar structures and they are not shown.

is included in the calculation of electronic structure, unless otherwise specified. The single Bi(111) bilayer has the point group symmetry of  $D_{3d}$  with spatial inversion included. As shown in Fig. 1, the top view of Bi(111) bilayer shows a bipartite honeycomb lattice with A and B sublattices. Two sublattices have different heights, forming bilayer structure. The calculated nearest-neighbor bond angles in single Bi bilayer is  $91^\circ$  and the lattice constant  $a = 4.34 \text{ \AA}$ . Based on the electronic structure of Bi bilayer (See S.I. [23]), the band inversion takes place between  $p$ -like valence and conduction bands at  $\Gamma$  point, leading to a 2d topological insulator with an indirect band gap of 0.5 eV, agreeing with the previous results [5–7].

To investigate the edge properties of the Bi(111) nanoribbons, we study two representative model systems: (1) a 40-atom (per unit cell) zigzag nanoribbon (about 7.3 nm wide), and (2) 50-atom (per unit cell) armchair nanoribbon (about 5.2 nm wide) (Fig. 1). For nanoribbons with native edges, the band structures are shown in the left panels of Figs. 2 (a) and (b). All bands remain spin-degenerate, owing to simultaneous time-reversal and inversion symmetry. Within the bulk band gap, the upper non-trivial and the lower trivial edge states are present simultaneously, which span the entire Brillouin zone (BZ). There are odd numbers of Kramers pairs of edge states at the Fermi level, showing that Bi(111) bilayer is indeed a 2d topological insulator. If we sweep the chemical potential across the gap by external gating, the number of conducting channel may change from 3 to 1 (or from 1 to 3). Here, the edge states do not show linear dispersion near  $\Gamma$  point, in contrast to Kane-Mele model of quantum spin Hall effect[4].

Given that the atomic edge adsorption of graphene nanoribbon has been achieved via hydrogen plasma etching recently and the edge decoration has important effects on electronic properties of graphene nanoribbons [24–26], the edge states of Bi(111) nanoribbon may be modified by chemical adsorption. We study the adsorption of hydrogen and iodine atoms on Bi(111) zigzag and armchair nanoribbons. Considering different adsorption sites from the edge to the middle part of nanoribbons (Fig. S2 in S.I. [23]), the atom adsorption on the outmost bismuth atom is the most stable structure with the lowest adsorption energy [23], compared with atom adsorption on the basal plane. It will lead to selective edge decoration in experiment, similar with graphene nanoribbon [26]. The adatoms restore three-fold coordination of the bismuths at two edges, indicating that the dangling bonds become saturated.

The middle and right panels in Figs. 2 (a) and (b) show the band structure after the edge functionalization for zigzag and armchair nanoribbons, respectively. Compared with native nanoribbons, there are only linear dispersing non-trivial edge states in the center of BZ, while the trivial edge states are removed. The Fermi velocities are  $8.5 \times 10^5 m/s$  and  $7.9 \times 10^5 m/s$  for hydrogen-

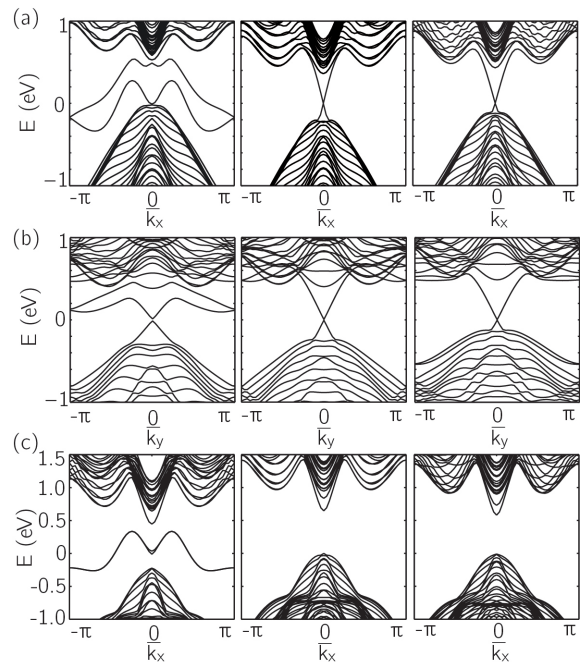


FIG. 2. The band structure of Bi(111) nanoribbons. (a) The zigzag nanoribbons with SOC. (b) The armchair nanoribbons with SOC. (c) The zigzag nanoribbons without SOC. The armchair nanoribbons without SOC are shown in Fig. S3. There are three panels in each figure. Left panel: The native edge. Middle panel: The hydrogen-terminated edge. Right panel: The iodine-terminated edge. The highest occupied energy level is set to zero energy.  $\bar{k}_x \equiv k_x a$  and  $\bar{k}_y \equiv \sqrt{3} k_y a$ .

and iodine-terminated zigzag nanoribbon, respectively. And the values are  $7.7 \times 10^5 m/s$  and  $7.3 \times 10^5 m/s$  for hydrogen- and iodine-terminated armchair nanoribbon, respectively.

The band structures Fig. 2(c) and Fig. S3 further show the corresponding band structure of Bi(111) nanoribbon without considering SOC. For the native edge, the edge states within the bulk gap are trivial ones in the absence of SOC. With atom adsorption at two edges, the trivial edge states are removed from the bulk gap. Therefore, taking into account SOC in our calculation, the emergent edge states (the middle and right panels in Figs. 2(a) and (b)) after chemical decoration are only non-trivial ones, resulting from the band inversion of TI.

Considering the significant modification of the edge bands by chemisorption, we suggest the effects of the edge engineering can be directly probed by transport and optical measurements. The key effect of the edge chemisorption is turning the number of edge conduction channels from three in the native nanoribbon to only one. This creates an interesting experimental apparatus to assess the effects of localization in the Anderson’s paradigm. We expect that in the case of single non-trivial edge channel, the conduction will stay quantized and will not be affected by non-magnetic disordered Anderson scatterers.

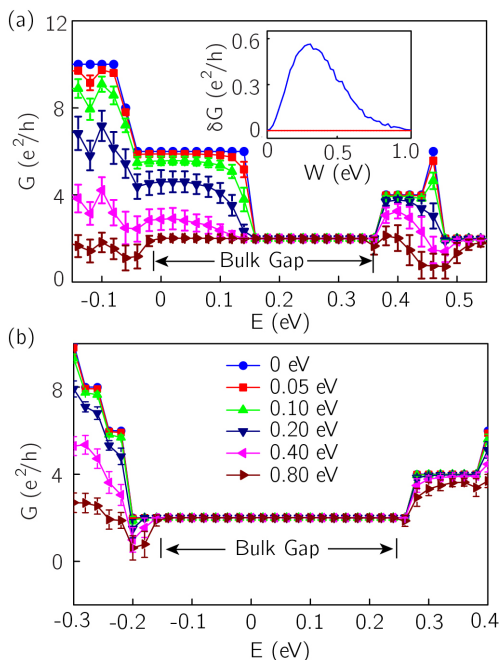


FIG. 3. Conductance,  $G$ , as the shift of the chemical potential for (a) the native and (b) hydrogen-terminated zigzag nanoribbon. Under Anderson disorders of different strengths  $W$ , the conductances of the nanoribbons are shown in different colors and symbols. The bar on every data point represents the conductance fluctuation,  $\delta G$ . The inset of (a) shows the conductance fluctuation as a function of  $W$ . The Fermi level is set to zero energy. The blue line stands for the edge states at 0.05 eV. The red line stands for the ones at 0.25 eV, which keeps zero.

On the other hand, the simultaneous presence of both non-trivial and trivial edge channels will show rather different transport behavior. Sufficiently strong disorder will eventually localize the trivial channels. However, in the intermediate localization regime, we may have window to detect disorder-induced conductance fluctuation [18]. The edge modification will also change the optical absorption of the material, which can also be measured experimentally. We therefore compute the transport and optical spectra of Bi(111) bilayer nanoribbons, based on a full-valence tight-binding (TB) model from DFT calculations [23].

Taking Bi(111) zigzag nanoribbon as an example, the transport spectra are calculated with the non-equilibrium Green's function approach [27]. For the native zigzag nanoribbon, the conductance is  $6e^2/h$  at the Fermi level, as expected and also consistent with experimental measurement [19]. The conductance of edge states changes from  $6e^2/h$  to  $2e^2/h$  as the chemical potential is gated up within the bulk band gap, leaving only the contribution from the non-trivial edge state. Upon introduction of Anderson disorder to the model, the conductance from trivial edge gradually decays with the increasing strength of disorder in the neighboring of the Fermi level

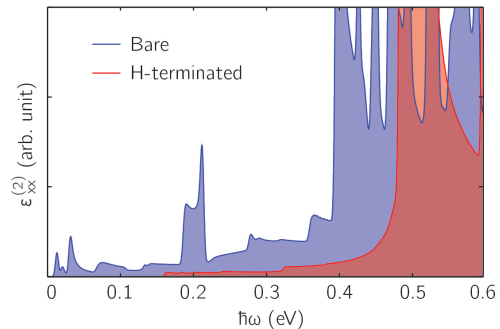


FIG. 4. The imaginary part of the dielectric tensor component,  $\varepsilon_{xx}^{(2)}(\omega)$ , as a function of the optical frequency  $\omega$  for zigzag nanoribbon. The bare edge and the hydrogen-terminated edge are shown in blue and red, respectively.

(Fig. 3(a)), indicating localization. At the same time, we indeed observe significant conductance fluctuation,  $\delta G$ . We see that  $\delta G$  first increases with weak Anderson disorder, but eventually decreases to zero upon complete localization of trivial edge channels (the inset of Fig. 3(a)). For hydrogen-termination zigzag nanoribbon, the conductance stays at the quantized platform of  $2e^2/h$  without any fluctuations within bulk band gap, as shown in Fig. 3(b). We also investigate the effect of less-than-full adsorption along two edges of nanoribbon with random occupancy of the adsorbed hydrogen atoms. It is found that 25% coverage of the edges with hydrogen adsorption can obtain a similar conductance plateau of  $2e^2/h$  as the one of 100% hydrogen adsorption, showing that it is feasible to improve the transport properties by partial edge decoration.

Fig. 4 shows the imaginary part of the dielectric tensor component for zigzag nanoribbon,  $\varepsilon_{xx}^{(2)}(\omega)$ , under the  $x$ -polarized irradiation field. Without any terminations, nonzero dielectric function shows that there are always optical transitions between edge states or between edge states and bulk states. However, these transitions are inhibited to a great extent for hydrogen-terminated zigzag nanoribbon. These observable characteristics can be used as signals of the edge decoration of Bi nanoribbons.

Alongside with the change of the band structure and the corresponding experimental signatures, the penetration depth and spin texture of edge states have been modified by edge engineering. Fig. 5(a) shows the change of the penetration depth with atomic adsorption for zigzag nanoribbon. For the zigzag nanoribbon with native edge, only one band of each group of the spin-degenerate edge bands are presented in the half of the BZ ( $k_x a$  from  $-\pi$  to 0), while other states can be obtained by the inversion and time-reversal symmetry. For hydrogen-terminated nanoribbon, the edge states are presented in the smaller zone of the BZ ( $-\pi/5$  to 0) to zoom in on the linear dis-

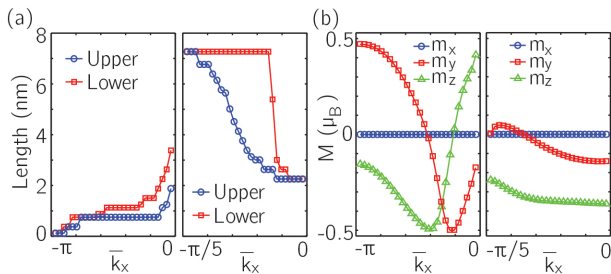


FIG. 5. The electronic properties of Bi(111) zigzag edge states. (a) The penetration depth of the edge states as a function of the momentum  $k_x$ . Left: The native edge. Right: The hydrogen-terminated edge. The upper and lower edge states are shown by blue circle and red square, respectively. (b) The spin texture of edge states. The blue circle, red square and green triangle stand for three components of spin moment,  $m_x$ ,  $m_y$  and  $m_z$ , respectively.  $\bar{k}_x \equiv k_x a$ . In (b), Only the more localized edge state (the upper edge) are shown, while the other one behaves in the same manner.

persion. The penetration depth is very short for both the upper non-trivial (blue circle in the left panel of Fig. 5(a)) and lower trivial edge states (red square) of the 7.3 nm-width nanoribbon without any termination. For states away from the bulk states ( $k_x a$  near  $\pi$ ), they are localized within 1nm closest to the edge. When the edge state approaches the bulk states ( $k_x a$  near 0), the penetration depth is gradually getting longer. In contrast, the penetration depths of the hydrogen-terminated edge states are all more than 2 nm, much longer than the one of native edge, which agrees with the inverse relationship between the penetration depth and the momentum-space width of the edge state [6, 28]. Besides, the penetration depths is also getting longer for hydrogen-terminated edge, as the edge state approaches the bulk states ( $k_x a$  from 0 to  $\pi/5$ ).

The spin moments,  $m_x$ ,  $m_y$  and  $m_z$ , for Bi(111) zigzag nanoribbon are shown in Fig. 5(b). Compared with Kane-Mele model [4] and HgTe/CdTe quantum wells [8], the edge states of Bi(111) nanoribbons have more complicated spin textures. For native zigzag nanoribbon, the components,  $m_y$  and  $m_z$ , perpendicular to the momentum  $k_x$  of zigzag edge, vary gradually and the spin direction rotates with the momentum. The component  $m_x$ , parallel to the momentum, is zero. It is similar to the interface state of well-known topological insulators, such as the natural cleavage (111) surface of Bi<sub>2</sub>Se<sub>3</sub>, where the spins are locked to their momentums at right angles [1]. For hydrogen-terminated zigzag edge,  $m_y$  and  $m_z$  have altered their trends and varied slowly in the momentum space near the Dirac point, with  $m_x = 0$ . The armchair edges have similar spin textures with zigzag edges, where  $m_x$  is still zero, as shown in Fig. S4 [23]. Given that the momentum direction is along y axis for armchair edges, the spin is no longer perpendicular to the momentum, in contrast with the spin-momentum orthogonality in well-

known TIs [1, 4, 8]. This departure can be explained by our effective model of single Bi(111) bilayer.

We suggest a low-energy effective Hamiltonian of single Bi(111) bilayer based on the symmetry analysis. Considering the inversion symmetry of single bilayer, we combine the  $p$ -orbitals near the Fermi level to form the bonding and anti-bonding states with definite parity,  $|p_\lambda^\pm\rangle = \frac{1}{\sqrt{2}}(|p_{A,\lambda}\rangle \mp |p_{B,\lambda}\rangle)$ , where  $p_\lambda = p_{x,y,z}$  stand for three  $p$ -orbitals and A/B for A/B sublattice stands of the honeycomb lattice. The superscript  $\pm$  correspond to even and odd parity, respectively. Taking into account the band splitting from both crystal field and SOC, the band inversion mainly arises between degenerate states  $|p_z^-, \pm\frac{1}{2}\rangle$  and degenerate states  $|p_{x,y}^+, \pm\frac{3}{2}\rangle$  near  $\Gamma$ , where  $\pm\frac{1}{2}$  and  $\pm\frac{3}{2}$  denote the corresponding total azimuthal quantum numbers.

We then construct four Wannier bases,  $|\alpha^-\rangle$ ,  $|\beta^+\rangle$ ,  $\hat{T}|\alpha^-\rangle$ , and  $\hat{T}|\beta^+\rangle$ , to describe the low-energy excitations of single Bi(111) bilayer, where  $|\alpha^-\rangle = |p_z^-, \frac{1}{2}\rangle$  and  $|\beta^+\rangle = N_0(|p_{x,y}^+, \frac{3}{2}\rangle + \eta|p_{x,y}^+, -\frac{3}{2}\rangle)$ .  $\hat{T}$  is time-reversal operator,  $N_0$  is the normalization factor and  $\eta$  is the weight factor (See details in S.I. [23]). The effective Hamiltonian near  $\Gamma$  is separated into two subblocks as below,

$$\mathcal{H}(\mathbf{k}) = \begin{bmatrix} H(\mathbf{k}) & 0 \\ 0 & H^*(-\mathbf{k}) \end{bmatrix}, \quad (1)$$

$$H(\mathbf{k}) = m[\sigma_z + k^2(\lambda^2\sigma_0 - \xi^2\sigma_z)] + \hbar v(k_x\sigma_x - k_y\sigma_y), \quad (2)$$

where  $\sigma_i$  ( $i = x, y, z, 0$ ) is the Pauli matrices addressing the subspace spanned by  $|\alpha^-\rangle$  and  $|\beta^+\rangle$ . The parameters  $m = 0.291$  eV,  $\lambda = 14.11$  Å,  $\xi = 15.51$  Å, and  $v = 1.079 \times 10^6$  m/s, which are obtained by fitting the DFT band structure of Bi(111) bilayer near  $\Gamma$  point, as shown in Fig. S1 [23]. The Hamiltonian leads to topological edge states with clean linear dispersion and a Fermi velocity of  $6.0 \times 10^5$  m/s, agreeing with our first-principle results. Moreover, when spin Pauli matrix  $s_x$  acts on the bases, we have  $\langle\varphi|s_x|\varphi\rangle = 0$ , where  $\varphi = \alpha^-, \beta^+$ . That is, the low-energy bulk bands have vanishing  $m_x$ , and so do the topological edge states of both zigzag and armchair edges, which arise from the bulk band inversion. In contrast, nonzero  $m_y$  and  $m_z$  can also be obtained by the Hamiltonian [23]. This explains the distinctive spin-momentum relationship in Bi(111) bilayer.

In conclusion, the edge chemical decoration of Bi(111) bilayer can significantly modify topological edge states. The experimental signatures and the low-energy effective Hamiltonian are also proposed. Clean edge state and model Hamiltonian will facilitate further investigations on topological properties of the Bi(111) bilayer, such as superconducting proximity effect [29] and topological Anderson Insulator [30].



*Acknowledgements.*— This work is supported by the National Science Foundation of China under Grants Nos. 11174009 and 11374219, by China 973 Program Projects 2013CB921900.

---

\* Equal contribution.

† jfeng11@pku.edu.cn

- [1] M. Z. Hasan and C. L. Kane, *Rev. Mod. Phys.* **82**, 3045 (2010).
- [2] X.-L. Qi and S.-C. Zhang, *Rev. Mod. Phys.* **83**, 1057 (2011).
- [3] J. E. Moore, *Nature* **464**, 194 (2010).
- [4] C. L. Kane and E. J. Mele, *Phys. Rev. Lett.* **95**, 226801 (2005).
- [5] S. Murakami, *Phys. Rev. Lett.* **97**, 236805 (2006).
- [6] M. Wada, S. Murakami, F. Freimuth, and G. Bihlmayer, *Phys. Rev. B* **83**, 121310 (2011).
- [7] Z. Liu, C.-X. Liu, Y.-S. Wu, W.-H. Duan, F. Liu, and J. Wu, *Phys. Rev. Lett.* **107**, 136805 (2011).
- [8] M. König, S. Wiedmann, C. Brüne, A. Roth, H. Buhmann, L. W. Molenkamp, X.-L. Qi, and S.-C. Zhang, *Science* **318**, 766 (2007).
- [9] I. Knez and R.-R. Du, *Front. Phys.* **7**, 200 (2012).
- [10] T. Hirahara, G. Bihlmayer, Y. Sakamoto, M. Yamada, H. Miyazaki, S.-i. Kimura, S. Blügel, and S. Hasegawa, *Phys. Rev. Lett.* **107**, 166801 (2011).
- [11] T. Hirahara *et al.*, *Phys. Rev. Lett.* **109**, 227401 (2012).
- [12] F. Yang *et al.*, *Phys. Rev. Lett.* **109**, 016801 (2012).
- [13] N. Fukui, T. Hirahara, T. Shirasawa, T. Takahashi, K. Kobayashi, and S. Hasegawa, *Phys. Rev. B* **85**, 115426 (2012).
- [14] L. Miao *et al.*, *Proc. Natl. Acad. Sci.* **110**, 2758 (2013).
- [15] Z. Wang, M.-Y. Yao, W. Ming, L. Miao, F. Zhu, C. Liu, C. Gao, D. Qian, J.-F. Jia, and F. Liu, *Nature Commun.* **4**, 1384 (2013).
- [16] L. Fu and C. L. Kane, *Phys. Rev. B* **76**, 045302 (2007).
- [17] D. Hsieh, D. Qian, L. Wray, Y. Xia, Y. S. Hor, R. Cava, and M. Z. Hasan, *Nature* **452**, 970 (2008).
- [18] D. Li and J. Shi, *Phys. Rev. B* **79**, 241303 (2009).
- [19] C. Sabater, D. Gosálbez-Mart, J. Fernández-Rossier, J. G. Rodrigo, C. Untiedt, and J. J. Palacios, *Phys. Rev. Lett.* **110**, 176802 (2013).
- [20] W. Kohn and L. J. Sham, *Phys. Rev.* **140**, A1133 (1965).
- [21] G. Kresse and J. Furthmüller, *Phys. Rev. B* **54**, 11169 (1996).
- [22] G. Kresse and D. Joubert, *Phys. Rev. B* **59**, 1758 (1999).
- [23] Online supporting information.
- [24] E.-j. Kan, Z. Li, J. Yang, and J. Hou, *J. Am. Chem. Soc.* **130**, 4224 (2008).
- [25] K. P. Loh, Q. Bao, P. K. Ang, and J. Yang, *J. Mater. Chem.* **20**, 2277 (2010).
- [26] X. Zhang *et al.*, *ACS nano* **7**, 198 (2012).
- [27] Y. Meir and N. S. Wingreen, *Phys. Rev. Lett.* **68**, 2512 (1992).
- [28] B. Volkov and O. Pankratov, *JETP Lett.* **42**, 178 (1985).
- [29] L. Fu and C. L. Kane, *Phys. Rev. Lett.* **100**, 096407 (2008).
- [30] J. Li, R.-L. Chu, J. K. Jain, and S.-Q. Shen, *Phys. Rev. Lett.* **102**, 136806 (2009).